Beyond Hopkinson's bar

F. Pierron[1], H. Zhu[1,2], C. Siviour[3]

[1] Faculty of Engineering and the Environment, University of Southampton, Highfield, SO17 1BJ, Southampton, UK
[2] Troyes University of Technology, 12, rue Marie Curie, BP 2060, 10010 Troyes cedex, France
[3] Department of Engineering Science, University of Oxford, Parks Road, Oxford, OX1 3PJ, UK

Keywords: high strain rate, full-field measurements, high speed imaging, Virtual Fields Method

Abstract

In order to perform experimental identification of high strain rate material models, engineers only have a very limited toolbox based on test procedures developed decades ago. The best example is the so-called Split Hopkinson Pressure Bar (SHPB) based on the bar concept introduced 100 years ago by Bertram Hopkinson to measure blast pulses. The recent advent of full-field deformation measurements using imaging techniques has allowed novel approaches to be developed and exciting new testing procedures to be imagined for the first time. One can use this full-field information in conjunction with efficient numerical inverse identification tools such as the Virtual Fields Method (VFM) to identify material parameters at high rates. The underpinning novelty is to exploit the inertial effects developed in high strain rate loading. This paper presents results from a new inertial impact test to obtain stress-strain curves at high strain rates (here, up to 3000 s^1). A quasi-isotropic composite specimen is equipped with a grid and images are recorded with the new HPV-X camera from Shimadzu at 5 Mfps and the SIMX16 camera from Specialized Imaging at 1 Mfps. Deformation, strain and acceleration fields are then input into the VFM to identify the stiffness parameters with unprecedented quality.

1 Introduction

In many areas of engineering, materials suffer deformation at high rates. This is the case when structures undergo impact, crash, blast, etc. but also in material forming like stamping or machining for instance. Another important area concerns biological tissues. For instance, traumatic brain injuries (TBI) involve damage of brain tissues caused by their high rate deformation following impact loading of the skull. Thanks to the spectacular progress of computing power and computational mechanics, it is now possible to perform extremely detailed numerical simulations of many complex situations where materials deform at high rates, with the objective to design safer structures, assess tissue injuries or devise more effective manufacturing processes, among others. However, to deliver their full potential, these computations require the input of reliable mechanical constitutive models of the materials loaded at high strain rates. This is an extremely challenging problem because of both the dynamic nature of the mechanical fields and the technological difficulties associated with strain metrology. Many dynamic test procedures have been devised within the last century, as reported in the review by Field et al. [9] with pioneering work of Hopkinson celebrated in this special issue dating back to 1914 [17], and its adaptation to the double bar system known as the Split Hopkinson Pressure Bar (SHPB) or Kolsky bar [21]. It is beyond the scope of the current paper to review in detail the different types of high strain rate tests and the reader is referred to [9]. However, all these test methods share common features and an important one is that they are all based on very limited experimental information. Indeed, the Kolsky bar uses strain gauges and a material with known elastic modulus to derive a global stress and strain response of the specimen. The spalling test used for concrete materials [7] uses point-wise Doppler laser velocimetry on the free specimen face as well as strain gauges bonded onto the specimen to infer the dynamic failure tensile stress using an analytical expression arising from simple 1D stress propagation [32, 33]. The Taylor impact test [51] relies on post-mortem measurement of the permanent change of shape of the test piece projectile, although it has also been used with in-situ high speed photography, see *e.g.* [56]. The very limited availability of experimental information forced experimentalists to be inventive and design test procedures that would be sufficiently simple so that this information could be used to infer information on the material constitutive properties. As such, they are the dynamic counterparts to the universal uniaxial tensile test or other simple statically determined tests. Going back to the SHPB test, which is certainly the most popular high strain rate testing technique as shown in Figs. 6 in [9, 53], while it has proved invaluable in obtaining information on the high strain rate behaviour of a very wide range of materials, it suffers from intrinsic limitations arising from the poor experimental information it uses. First, the test is restricted to uniaxial loading and relies on the assumption of homogeneous stress and strain states. This prevents a more complete constitutive law identification using heterogeneous stress states. Also, the effect of transient stress waves has to be controlled, usually leading to very short test specimens. In the general case, this cannot always be achieved easily, particularly for soft materials. There is a very large literature on such effects, see [26] for instance.

The recent advent of inexpensive and powerful imaging devices (CCD or CMOS sensors) coupled to automated image processing tools has led to new fully digital instrumentation capable of acquiring deformation at a great number of points, hence the terminology 'full-field' measurements. This type of measurement technique typically provides from several hundreds to several tens of thousands of independent deformation measurement points. The most representative example of this is the so-called 'Digital Image Correlation' [49] (and its 3D counterpart using stereovision) which has seen exponential diffusion within the last decade, thanks to the availability of plug-and-play commercial systems. Many researchers in high strain rate testing of materials see this as a great opportunity, as reported in [9]. Most of the applications currently published deal with simple uniaxial tests. In this case, the most basic use of the full-field data consists in using it as a non-contact strain gauge by averaging the strains over the field of view, see for instance [11, 20, 23, 24, 55], while checking that the strain field was reasonably uniform. Such measurements have also been used to have better insight into strain localization in uniaxial tests [6, 50]. More rarely, the full-field data has been used to identify a model using a uniform stress approach [50] or finite element model updating [18, 19, 25]. It is to be noted that large strains (metals in plastic deformation or polymers) are usually measured, which is in the favourable end of the DIC usage range. However, such simple tests do not make the most of the rich full-field strain information and the current authors agree with this statement from [11]:

> "In the past, the use of the SHB technique was limited for testing specimens undergoing uniform deformation. The introduction of 3D image correlation for measuring the full strain field on the surface of the specimen provides means for developing new types of experiments with the SHB technique in which the deformation in the specimen is intentionally not uniform."

More rarely, such test specimens with more complex shapes leading to heterogeneous stress/strain states have been considered [13,28,35], either with a view to validating FE models [35] or to identify constitutive models using finite element model updating techniques [36] or the Virtual Fields Method [4, 31]. Finally, most of the previous examples deal with quasi-static situations, meaning by this that transient inertial effects have vanished when the data are processed. In fact, it is even a strong requirement for the standard SHPB analysis. Some authors have studied materials in situations where stress waves were still propagating, either to investigate the behaviour of low-impedance materials [30, 54] or to provide stiffness measurements [48]. For stiff engineering materials however, imaging in this range requires the use of ultra-high speed imaging, as defined in [43], because of the very large wave speeds (several $km.s^{-1}$).

If full-field strain measurements clearly bring important additional information in the above examples, a global force measurement is always required to obtain constitutive parameters (except when stress waves are propagating, [30,48], which connects to the current paper). If external force measurement in quasi-static is easy thorough load cells, inertial effects spoil such measurements in dynamics ('ringing' effects). This is the reason for the Hopkinson bar which is basically a load cell designed to work in a particular set of conditions (1D wave propagation, elastic deformation of the bar etc.). This constraint for external impact load measurement is one of the main constraints on the design of current test configurations.

However, looking at other areas of engineering, there are examples of dynamic testing where material constitutive parameters can be retrieved without any external load measurements. For instance, ultrasonic testing uses measured wave speeds to derive elastic stiffness components, even though the associated metrology does not allow for spatial resolution and is limited to elasticity. An extension of this idea can be found in Magnetic Resonance Elastography [29] where MRI-based measurement of bulk dynamic strain fields are combined with the wave equation to provide a spatial map of shear modulus. This however requires the use of an inverse solution which has led to much research, [45, 47] for instance. The idea is similar in [30] but the analysis is simpler due to the uniaxial nature of the test. In both cases, the acceleration information serves as a load cell, and the load cell gauge factor is the material density. Finally, several studies have shown that elastic [14, 15] and viscoelastic [12] stiffness components could be identified from full-field measurements and the Virtual Fields Method [39] using the inertial forces as load cell.

The objective of this article is to propose a general procedure to exploit dynamic impact tests using full-field strain and acceleration measurements in order to identify constitutive material parameters. The key idea is to fully exploit the full-field information so that the constraint for external impact force measurement is relieved thanks to the use of inertial loads as an effective load cell. The first part of the article is more didactic; it presents the current state-of-the-art and uses a simple example as a demonstration. The second part of the paper is dedicated to the design of a new purely inertial test. Optimized special virtual fields extended to dynamics from [2] are briefly presented and validated from simulated measurements. In the third part, an experimental validation is presented using two different ultra-high speed cameras. Finally, conclusions and perspectives are provided, opening the way for a new generation of dynamic high strain rate tests beyond Hopkinson's bar.

2 Acceleration as a load cell

In order to illustrate the concept of using acceleration maps in the material identification process, the simple test configuration in Fig. 1 is considered. This is the typical situation of a specimen loaded in an SHPB apparatus. The problem is considered as a 2D plane stress one (thin specimen of thickness h) and Voigt contracted index notations are used. The forces acting on its two boundaries are defined as:

$$F_1(t) = -h \int_{-b/2}^{b/2} \sigma_1(x_1 = 0, x_2, t) dx_2 \ ; \ F_2(t) = h \int_{-b/2}^{b/2} \sigma_1(x_1 = L, x_2, t) dx_2 \tag{1}$$

In order to simplify the writing of the equations, the time variable will be omitted in the rest of the paper but all mechanical fields do depend on time even if time is not mentioned. Writing the global dynamic equilibrium of the solid, the following equation is obtained in the x_1 direction:

$$F_1 + F_2 = \rho h \int_0^L \int_{-b/2}^{b/2} a_1 dx_1 dx_2 \tag{2}$$

This can be obtained by writing the equilibrium of a thin transverse slice and integrating it along x_1 as in [1, 34]. In practice, if full-field displacements are obtained as a function of time with sufficient spatial and temporal resolution, then the second term of this equation can be calculated as:

$$\int_0^L \int_{-b/2}^{b/2} a_1 dx_1 dx_2 \approx \sum_{i=1}^{n} a_1^{(i)} s^{(i)} \tag{3}$$

where $a_1^{(i)}$ is the acceleration value at data point number i, $s^{(i)}$ is the small surface associated with measurement at data point number i and n is the total number of measurement points. Obviously, the quality of this approximation is highly dependent on both the spatial frequency contents of the acceleration field and the density of the full-field measurements. Since most of the time, the displacement data are obtained over a regular grid a with Digital Image Correlation (DIC), then the discretized acceleration term can be written as:

$$\sum_{i=1}^{n} a_1^{(i)} s^{(i)} = Lb\overline{a_1} \tag{4}$$

where the overline indicates geometrical spatial averaging over the field of view. The final equation is therefore:

$$F_1 + F_2 = \rho V \overline{a_1} \tag{5}$$

where V is the volume of the field of view. This very simple equation, valid at any time t during the test, is very powerful in practice. For instance, if the force is obtained at one end of the specimen, either F_1 or F_2, then average stress profiles can be reconstructed at any x_1 location thanks to this equation, provided that the density is known. Othman et al. [1, 34] have used it to identify the behaviour of a synthetic rubber material. They used a single output bar to measure F_1 and F_2 was applied by an un-instrumented projectile. They were able to calculate average true stress profiles and produce true stress/strain curves at different locations along the test specimen, demonstrating the power of the approach.

A very similar application was recently published by Pierron and Forquin [38]. It concerned a spalling test on a cylindrical concrete specimen. One end was connected to a Hopkinson bar producing a compressive pulse. This compressive pulse travels along the specimen and is reflected off the free end into a tensile pulse. The shaping of the pulse and the specimen length were such that the specimen underwent tension after reflection and fractured then. This is basically an indirect tensile test usually exploited from strain gauge measurements on the bar to produce the impact force, strain gauges on the specimen to monitor the strain rate and measure modulus from the wave speed and point measurement of the velocity at the free end to identify the dynamic failure stress from Novikov's formula [7]. Referring back to Fig. 1, in this case, $F_2 = 0$ as $x_1 = 0$ represents the free end. Starting from the free end as the known force (which is zero), average stress profiles were reconstructed from:

$$\overline{\sigma_1(x_1, t)} = \rho x_1 \overline{a_1(x_1, t)} \tag{6}$$

It should be noted that in this case, no external force is needed at all, or more accurately, one force measurement is needed but provided by the free end condition. The results thus obtained enabled local stress-strain curves and Young's modulus values to be derived as well as another estimate of the dynamic fracture stress. Interestingly, this value did not match the Novikov one. Only later was the reason for this disclosed as a difference between tensile and compressive Young's modulus caused by the presence of initial micro-cracks [10].

The previous approach is very simple and powerful but unfortunately, it is restricted to some very simple quasi-uniaxial tests. It can be extended to a shear force at both ends (*i.e.* a set of vertical forces) or a bending moment. But let us now imagine that neither F_1 nor F_2 are measured. This would happen in an SHPB set-up if no strain gauges on the bars were used, for instance. The previous analysis would then produce an equation with two unknowns, which would be useless. However, it is possible to extend this simple analysis by introducing the principle of virtual work.

3 Extension to more general cases: the VFM

3.1 The Virtual Fields Method

The general equation for the principle of virtual work is:

$$\underbrace{-\int_{V_m} \underline{\underline{\sigma}} : \underline{\underline{\epsilon}}^* dV}_{Internal\, virtual\, work} + \underbrace{\int_{\partial V_m} \overrightarrow{T}.\overrightarrow{u}^* dS}_{External\, virtual\, work} = \underbrace{\int_{V_m} \rho \frac{\partial^2 \overrightarrow{u}}{\partial t^2}.\overrightarrow{u}^* dV}_{Acceleration\, virtual\, work} \tag{7}$$

where:

- ∂V_m is the boundary surface of the volume V_m,
- $\overrightarrow{T}$ is the Cauchy stress vector acting at the boundary surface ∂V_m,
- $\underline{\underline{\sigma}}$ is the Cauchy stress tensor,
- $\overrightarrow{u}^*$ is a C^0 vectorial function referred to as "virtual displacement field",
- $\underline{\underline{\epsilon}}^*$ is the virtual strain tensor derived from $\overrightarrow{u}^*$ ($\underline{\underline{\epsilon}}^* = \frac{1}{2}(\underline{\underline{\text{grad}}}(\overrightarrow{u}^*) +^T \underline{\underline{\text{grad}}}(\overrightarrow{u}^*))$,
- ρ is the material density,
- ":" and "." are the dot products respectively between matrices and vectors.

This equation is the integral form of the local stress equilibrium equation. It is possible to use this equation to produce Eq. 5. Indeed, let us consider the following virtual field:

$$\left\{ \begin{array}{l} u_1^{*(1)} = 1 \\ u_2^{*(1)} = 0 \end{array} \right. \qquad \left\{ \begin{array}{l} \varepsilon_1^{*(1)} = 0 \\ \varepsilon_2^{*(1)} = 0 \\ \varepsilon_6^{*(1)} = 0 \end{array} \right. \tag{8}$$

Because of the zero virtual strain, the internal virtual work as defined above is zero. The external virtual work is produced by both F_1 and F_2. For both ends of the specimen, the virtual displacement is equal to 1, so the external virtual work is $F_1 + F_2$. Finally, because $u_2^{*(1)} = 0$, the acceleration virtual work only depends on the x_1 component and provides the same term as the right-hand side of Eq. 5, with $a_1 = \frac{\partial^2 u_1}{\partial t^2}$. By using the two following virtual fields, one could get similar equations for a shear force or a moment:

$$\text{Shear force} \qquad \left\{ \begin{array}{l} u_1^{*(1)} = 0 \\ u_2^{*(1)} = 1 \end{array} \right. \qquad \left\{ \begin{array}{l} \varepsilon_1^{*(1)} = 0 \\ \varepsilon_2^{*(1)} = 0 \\ \varepsilon_6^{*(1)} = 0 \end{array} \right. \tag{9}$$

$$\text{Moment} \qquad \left\{ \begin{array}{l} u_1^{*(2)} = x_2 \\ u_2^{*(2)} = -x_1 \end{array} \right. \qquad \left\{ \begin{array}{l} \varepsilon_1^{*(2)} = 0 \\ \varepsilon_2^{*(2)} = 0 \\ \varepsilon_6^{*(2)} = 0 \end{array} \right. \tag{10}$$

These virtual fields correspond to the three virtual rigid body fields that produce zero virtual strains. The resulting equations only involve end forces (or moments) and acceleration and can be used to produce stress-strain curves without the need to formulate a model *a priori*. This can be referred to as a non-parametric approach as quoted from [1,34]. But let us now imagine that neither F_1 nor F_2 are measured. These three rigid body like virtual fields are not useful anymore and one needs to resort to a more complex formulation that includes virtual deformation. If the end forces are unknown, it is possible to tailor a virtual field that will cancel out the contribution of these forces to the principle of virtual work. For instance, using the following virtual field:

$$\left\{ \begin{array}{l} u_1^{*(1)} = x_1(x_1 - L) \\ u_2^{*(1)} = 0 \end{array} \right. \qquad \left\{ \begin{array}{l} \varepsilon_1^{*(1)} = 2x_1 - L \\ \varepsilon_2^{*(1)} = 0 \\ \varepsilon_6^{*(1)} = 0 \end{array} \right. \tag{11}$$

The virtual displacement is zero for both ends at $x_1 = 0$ and $x_1 = L$. Therefore, the external virtual work is zero. The final equation arising from this virtual field is:

$$-\int_0^L \int_{-b/2}^{b/2} (2x_1 - L)\sigma_1 dx_2 = \int_0^L \int_{-b/2}^{b/2} \rho x_1(x_1 - L) a_1 dx_1 dx_2 \tag{12}$$

valid at any time t during the test. The key idea is now to substitute the σ_1 stress component using the constitutive equation. This requires the *a priori* selection of a model as with all inverse techniques, as opposed to the simple non-parametric approach above. Here, a simple isotropic linear elastic model is selected. For plane stress, the constitutive model depends on two stiffness components Q_{11} and Q_{12}: $\sigma_1 = Q_{11}\varepsilon_1 + Q_{12}\varepsilon_2$. Feeding this into Eq. 12 assuming the stiffness components to be constant and approximating the integrals by discrete sums (introducing the spatial average indicated by the overline), the final equation is obtained:

$$-Q_{11}\overline{(2x_1 - L)\varepsilon_1} - Q_{12}\overline{(2x_1 - L)\varepsilon_2} = \overline{\rho x_1(x_1 - L)a_1} \tag{13}$$

One can clearly see here the role of load cell played by the acceleration term. In a quasi-static situation, this equation would lead to zero equal to zero (uniform strain distribution and zero acceleration). In order to extract both stiffness components, another equation must be derived. For instance, the following virtual field can be used:

$$\left\{ \begin{array}{l} u_1^{*(1)} = 0 \\ u_2^{*(1)} = x_1(x_1 - L)x_2 \end{array} \right. \qquad \left\{ \begin{array}{l} \varepsilon_1^{*(1)} = 0 \\ \varepsilon_2^{*(1)} = x_1(x_1 - L) \\ \varepsilon_6^{*(1)} = (2x_1 - L)x_2 \end{array} \right. \tag{14}$$

leading to the following equation:

$$-Q_{11}\left[\overline{x_1(x_1 - L)\varepsilon_2} + 0.5\overline{(2x_1 - L)x_2\varepsilon_6}\right] - Q_{12}\left[\overline{x_1(x_1 - L)\varepsilon_1} - 0.5\overline{(2x_1 - L)x_2\varepsilon_6}\right] = \rho\overline{x_1(x_1 - L)x_2a_2} \tag{15}$$

This leads to a linear system of two equations with two unknowns that can be solved for Q_{11} and Q_{12}. This identification technique is known as the Virtual Fields Method (VFM) and has been applied over the past to a very wide range of materials and test configurations, including non-linear problems for which the resolution is performed through optimization of the difference between the terms in the principle of virtual work. It is beyond the scope of the current paper to detail this, the reader is referred to the recent book on this topic [39]. It should be noted that the equations above hold for any time at which a set of images is available. This leads to many estimates of these parameters, as long as there is significant acceleration. When the acceleration dies out, the linear system fails to produce the stiffness values, only Poisson's ratio can be obtained (ratio of the two stiffness components). This approach was validated experimentally on quasi-isotropic composite specimens loaded in a tensile split Hopkinson bar (SHB) apparatus and the grid method was employed to derive strain and acceleration fields. The method successfully provided estimates for the two stiffness components of this particular material [27], which was the first time such an approach was published to the best knowledge of the present authors. Two difficulties were identified however. First, the quality of the images provided by the ultra-high speed Cordin 550-62 rotating mirror camera was still wanting compared to more standard CDD cameras, leading to low signal to noise ratio measurements. This issue will be resolved as UHS cameras improve, which is already happening as illustrated in the experimental validation section of this paper. The second one relates to the test itself. The tensile SHB set-up produces significant accelerations during only the first 20 μs^{-1}. Since this SHB set-up was not specifically designed for the new data processing procedure presented here, and since this new procedure does not require any of the strong requirements of the SHB tests, a very wide design space opens up which needs to be explored. Up to now, only three different applications of the VFM at high strain rates have been published [27, 38, 41], more as feasibility studies. However, it was clear from these first experiences that inertial tests would be favourable. This is the route that is explored here.

3.2 Special optimized virtual fields

Before moving on to the inertial test described in this paper, a few words on the virtual fields selection are required. Indeed, there is an infinity of possible virtual fields and each of them, when input into Eq .7, will produce a different equation of the type of Eq. 13. As a consequence, a legitimate question is that of the choice of virtual fields. The first thing than can be said is that if the strain data are exact, any choice of independent virtual fields will lead to the same identified stiffness values. But if data are corrupted by noise, which is the case for experimental measurements, then different sets of virtual fields lead to different stiffness values. It was shown in [2, 3] that for a certain basis of functions used to expand the virtual fields (like polynomials, harmonic functions or piecewise functions like finite elements), there is a unique solution leading to the maximum likelihood solution. These virtual fields are called 'special optimized' and will be used in this paper, using bilinear finite element to expand the virtual fields, see [39]. It should be noted that this procedure also outputs coefficients called η_{ij} which relate the standard deviation of the strain noise to the standard deviation of the identified Q_{ij} stiffness components. This coefficient is interesting as it is an *a priori* estimator of the identification quality. This will be commented in the next section.

4 Validation on simulated data

In order to validate the procedure described above, experimental data have first been simulated by finite element computations. This is always the first step as the stiffness values entered in the model serve as perfect reference. A 2D plane stress isotropic constitutive model has been considered here in order to keep the number of unknowns low. This is also the law that will be identified in the experimental validation section. A 1-dimension inertial test is considered first. It is composed of a thin specimen of thickness 4×10^{-3} m impacted by a steel projectile of thickness also 4 mm, see Fig. 2. Due to the nearly uniform contact forces between the two solids, the stress wave propagation is nearly unidirectional. The response of this impacted isotropic specimen was simulated using ABAQUS/EXPLICIT to produce full-field strain and acceleration maps which were then processed by the VFM. The details of the finite element model are shown in Table 1. The mesh density is the result of the a convergence study.

From the results, it was found that contact time is about 17 μs for this model, which corresponds to the time needed for a return travel of the stress wave along the projectile, as expected. Full-field strain and acceleration maps has been output from ABAQUS. Fig. 3 presents the full-field strain and acceleration maps at 10 μs. As seen in Fig. 3, the acceleration levels in the specimen are high. This feature is used to extract the constitutive parameters using the VFM.

As previously stated in Section 3.2, bilinear piecewise functions are used to expand the virtual fields. The virtual mesh consists of 4 elements in the horizontal direction and 3 elements in the vertical direction. The virtual displacement vector along the contact boundary is set to 0 so that the virtual work of the impact force between the two solids is zeroed out from the VFM equation. The results will be expressed as Young's modulus and Poisson's ratio, related to the stiffness components Q_{11} and Q_{12} by:

$$\begin{cases} Q_{11} = \frac{E}{1-\nu^2} \\ Q_{12} = \frac{\nu E}{1-\nu^2} \end{cases} \tag{16}$$

The dynamic full-field strain and acceleration fields were then processed using the VFM. The identification of Young's modulus and Poisson's ratio are shown in Fig. 4.

In this figure, it is clear that the identification is very good, which validates the VFM programme as well as the forward FE calculations. The relative errors on the identified values are less than 1%. It is worth noting that the error on the identified Poisson's ratio at 1 μs is much larger. This is because at that time, the stress wave is concentrated in a very small area near the contact end, increasing the effects of numerical noise.

The optimized nature of the virtual fields defined here has been validated as follows. The FE strain maps have been polluted with white Gaussian noise of increasing standard deviations. For each noise level, 30 identifications have been performed using 30 different copies of the same noise. It is therefore possible to plot the coefficient of variation of each identified stiffness component as a function of strain noise level. This is reported in Fig. 5 in the form of a cloud of points of linear tendency fitted by a linear approximation. The slope of this approximation is an experimental evaluation of the η_{ij}/Q_{ij} provided by the optimized virtual fields routine. It is reported at the bottom of the plot as the 'fitted value', which is compared to the 'theoretical' one directly issued from the virtual field optimization procedure. As seen at the bottom of these plots, both values match very well, validating the optimized VF definition. According to [2], these coefficients of variation are the smallest possible among the virtual fields expanded over the current set of piecewise functions (4 x 3 virtual mesh). Now that the VFM routines are validated for this dynamic test, it is applied to real experimental data.

5 First experimental validation

5.1 Experimental set-up

A series of inertial tests according to Fig. 2 tests has been performed at the University of Oxford. A picture of the experimental set-up can be found in Fig. 6. The projectile is a steel cylinder of radius 34 mm and length 50 mm. It is launched by a gas gun to reach a nominal speed of 30 $m.s^{-1}$ for these experiments. The specimen is positioned at the end of the launch tube of the gas gun. It is resting on a foam stand that has been machined in an attempt to align the specimen with the projectile at the moment of impact. Two pieces of thin copper film were bonded onto the foam support right at the edge of the specimen so that when the projectile reaches, it contacts both pieces of film which closes an electrical circuit, providing the triggering signal. The specimen was cut to the dimensions of that in Fig. 2 from a carbon/epoxy laminated plate. The material used here is a 3.6 mm $[0/45/-45/90]_s$ carbon/epoxy laminate made from CYTEC's MTM58FRB prepreg. This prepreg is a 120 $°C$ cure system using high strength carbon fibres. It is mainly used in automotive applications like Formula 1, for instance. The nominal stiffness parameters obtained from quasi-static tests performed at the University of Southampton [22] are: E_{11} = 124 GPa, E_{22} = 7.5 GPa, ν_{12} = 0.31, G_{12} = 4.0 GPa. Since the lay-up is quasi-isotropic, the in-plane stiffness behaviour only depends on two elastic constants. Using lamination theory, this provides an in-plane Young's modulus E of 47.1 GPa and a Poisson's ratio of 0.31. because such lay-ups are heavily dominated by fibre behaviour and carbon fibres exhibit very low strain rate dependance, this quasi-static reference will be used as a target value for the current tests.

The strain measurement technique used here is the so-called 'grid method' [5, 40], also more recently referred to as sampling moiré [44]. A grid was transferred onto the specimens using the procedure described in [42]. The choice of the pitch of the grid depends on the spatial resolution of the camera used to record the images, which is detailed in the following.

5.2 Imaging set-up

Because it is required to calculate acceleration maps from the displacements, it is necessary to grab images with very low inter-frame times, of the order of the microsecond. This is the range of what Reu and Miller [43] define as ultra-high speed imaging. Here, two different cameras have been used in order to check the effect of image quality on the results. The first camera is a Specialized Imaging SIM 16. This is an intensified gated camera which principle relies on dividing the light into several optical paths, here, 16, and recording at very high rates by electronically gating the corresponding 16 CCD sensors sequentially. The fact that light is divided by as many channels as there are CCD sensors leads to the need for light amplification. Unfortunately, this causes a number of issues, including 'leakage' of light over neighbouring pixels, blurring the image and creating significant spurious strains. This is documented in [37, 52] for a similar camera using the same technology, the IMACON200, even if the current SIMX16 camera suffers slightly less from this problem. Finally, because of small misalignment of the different CCD sensors, displacements have to be calculated from images of each individual sensors. Therefore, a series of 16 images of the stationary specimen are first recorded before images of the deforming specimens are acquired and the first set of images is used as the undeformed reference for each sensor, as explained in [41, 52]. The second camera used here is a Shimadzu HPV-X, a recent version of the older HPV-1/2 series. This camera uses a dedicated sensor called In-Situ CCD (IS-CCD) which circumvents the issue of memory read-out by storing the data directly on the chip [8]. There are a number of issues with this sensor, as summarized in [37] but when used with the correct settings (dark image, avoid 1 Mfps frame rate), very good images can be captured as evidenced in [38]. The new sensor implemented in the Shimadzu HPV-X seems to suffer much less, if at all, from the issues noted on the previous generation cameras. It is not the objective here to perform a full characterization of the measurement performances using these cameras, only basic performance information is provided (see next section). Information concerning the imaging systems and grids is collated in Table 2.

5.3 Measurement results

From the raw grey level grid images, spatial phase maps relating to displacements are obtained using spatial phase shifting. The algorithm implemented here is called WDFT (Windowed Discrete Fourier Transform). Information about the grid method processing can be found in [5]. These phase maps may contain phase jumps from π to $-\pi$ when the displacement range in one image is larger than the grip pitch. This is known as 'phase wrapping'. Here, these maps have been unwrapped using the algorithm published by Herraez *et al.* [16]. Finally, because of the rigid body motion accompanying the stress wave propagation, the mean displacement as a function of time also exhibits 'jumps' each time the rigid body translation goes above the grid pitch. Since the rigid body movement is monotonic, simple temporal unwrapping is performed by adding integer numbers of pitch size to the displacement maps so that the mean displacement is monotonic. This is essential in dynamics to derive the acceleration maps.

Because of camera noise, spatial and temporal smoothing are necessary in order to reach the required resolution in both strain and acceleration. A sensitivity study has been undertaken which detailed results are beyond the scope of the present paper. The outcome is that strains have been calculated from displacements smoothed with a Gaussian filter over different windows of data points as reported in Table 2. As for the acceleration, it has been calculated from combined spatial and temporal smoothing as also reported in Table 2. The resolution values have been evaluated as the standard deviation of maps obtained from series of stationary images. The far superior image quality from the Shimadzu HPV-X camera is obvious on the raw displacement resolution, the only real advantage of the SIMX16 camera being its better spatial resolution, the limited total number of images being also a very stringent limiting factor.

Fig. 7 shows the average strain and acceleration profiles calculated over the whole field of view. Even though these tests were performed on two different days weeks apart, these plots look very much alike, even though the SIMX16 data is much noisier, as expected. One can see a shift of 2 μs between the two curves because of the difference in triggering. In order to get a feel for the results, displacement, strain and acceleration maps are provided at time 8 μs for the SIMX16 and 10 μs for the HPV-X so that the data correspond to the same state of the test

(Figs. 8 to 10). Videos of the whole set of data are available as supplementary material. Again, the maps are really similar, showing the same localization of the impact at the bottom. This illustrates the reproducibility of the set-up which uses a rigid foam stand for the specimen.. This means that better alignment of the set-up could also be possible to generate a more even impact. From these images and videos, the superior data quality of the data delivered by the HPV-X camera is spectacular. Looking at the acceleration maps, one can see values going up to nearly 1 million g's, which corresponds to what was obtained from the finite element calculations, see Fig. 3. As for the strain rate, Fig. 11 shows the average strain rate over the field of view as well as the strain rate map at 6 μs for the HPV-X test. The strain rate reaches a maximum value close to 3000 s^{-1} at the beginning of the test but with highly heterogeneous strain rate maps. Here, this strain rate information is just used to provide an idea of the order of magnitude reached in this test but it will not be used in the identification. This issue will be commented on later in the article. The next stage is to use these data in the identification process. This is presented in the next section.

5.4 Identification results

5.4.1 Non-parametric approach

The first approach used in the current work is that of Section 2. Average σ_1 stress along vertical lines have been reconstructed using Eq. 6. This enables to plot average σ_1 stress against average ε_1 strain at all vertical sections of the specimen. Since the test provides a dominantly unidirectional state of stress, the slope of this curve identifies Young's modulus of the quasi-isotropic specimen, as a first approximation. An example is provided in Fig. 12 for the SIMX16 test and in Fig. 13 for the HPV-X one, at 20.7 mm from the free edge (about two-thirds towards the right hand-side of the field of view). The first one is very noisy, as one would expect. Using a linear fit of the data, one recovers a value of 51.7 GPa for E, about 10 % higher than the expected value of 47.1 GPa. On Fig. 13(a), one can see that the stress strain curve from the HPV-X data is of much better quality and exhibits nice linearity except during the early stages of the test. This is caused by the temporal smoothing to obtain acceleration. It results in non-zero acceleration values before the wave reaches, leading to stress without any strain. After about 12 images (half the smoothing window of 25 images), correct data are recovered as seen on Fig. 13(b). In this case, a linear fit of the data leads to a Young's modulus of 40.1 GPa. This is 14 % lower than the expected value of 47.1 GPa. In order to check for the consistency of these results, stress-strain curves have been plotted in Fig. 14(a) for the unloading part of the response only, at three different locations in the field of view. The three curves are very similar, only the one at 20.7 mm exhibits an offset caused by the problem mentioned previously, which tends to decrease in intensity when moving closer to the free end, probably because the wave front is less sharp there. From this, a modulus around 40 GPa is recovered from the three sets of data, showing good consistency.

A legitimate question is whether the unidirectional stress assumption is reasonable. In order to investigate this issue, Fig. 14(b) represents the average σ_1 stress as a function of the average of $\varepsilon_1 + \nu\varepsilon_2$, the slope of which provides the Q_{11} stiffness component which relates to E through Eq. 16. One can also see good linearity of the response. Assuming a value of 0.31 for Poisson's ratio, one can they calculate E from Q_{11} and compare the results to that obtained using the uniaxial stress assumption. This is shown in Fig. 15, where data too close to both edges have been discarded. Indeed, close to the free edge, stress and strain become too low and close to the impact edge, issues with in-plane loading may occur. The results show that the difference between the two values is about 15 % for about half the field of view, closer to the free end. The value extracted from Q_{11} is the closest to the quasi-static reference, showing the limitations of the uniaxial stress assumption, as could have been expected from the heterogeneous nature of mechanical fields in the test. However, both approaches converge to a lower value of E towards the impact end of the specimen. It is not clear why this is happening but it is thought that the contact between the projectile and the specimen is not perfect and may lead to some through thickness strain heterogeneities. In this case, the strains may be too high on the front side where the measurements are performed but because the thickness of the specimen is small, the strains tend to average out through-the-thickness at a certain distance from the impact zone, a kind of St-Venant effect. This will need to be investigated in the future, through both finite element modelling and experimental improvement of the projectile to specimen contact. The same data for the SIMX16 is shown in Fig. 16. The variations in Young's modulus are much larger than for the HPV-X data and only the mean value over the field of view excluding the edges (shown in grey box on the figure) relate to the reference values. Clearly, the quality of the data is not good enough for this approach. The next section finally investigates the method presented in

Section 3 to extract both E and ν from the special optimized Virtual Fields Method.

5.4.2 Parametric VFM approach

The experimental data are now processed with the special optimized Virtual Fields Method as described in Section 3.2. A piecewise virtual mesh is used, with varying virtual elements m along x_1 and n along x_2. The field of view used in the identification discard 9 mm from the impact edge and 2.2 mm from the free edge for the reasons detailed above. The virtual nodes of the virtual mesh are all constrained to zero virtual displacements to filter out the unknown stress distributions at the boundaries of the field of view. Identification is performed at each time t when an image is recorded. The results reporting E and ν obtained from Q_{11} and Q_{12}, which are the quantities delivered by the VFM, for $m = 10$ and $n = 2$ are shown in Fig. 17. They are rather nice even though the data are bad for the early and late stages of the test. This is not surprising as strains are low at the beginning and at the end. This is illustrated by the η_{ij} parameters in Fig. 18. One can see high values at the beginning and end, reflecting bad signal to noise ratio then because of low strains. If one only keeps the data between 6 and 12 μs, then the average E is 47.2 GPa and the average ν is 0.28, which are very close to the reference. A legitimate question concerns the stability of the identification with respect to the virtual mesh. Figs. 19 and 20 answer this question. Stability is excellent, with a slight convergence effect when the virtual mesh density is increased and a saturation after 8 x 2. If the density was increased further. This is consistent with previous results on this [39]. Globally, the stability of the VFM approach is good even though some oscillations in stiffness parameters can be seen. Further work is required to investigate this issue in more depth, as is detailed in the conclusion.

6 Conclusion

While celebrating the 100th anniversary of the seminal article by Bertram Hopkinson [17], this paper presents a new paradigm in high strain rate testing which has the potential to remove the need for impact force measurement in dynamic testing in the future. Apart from simplifying the experimental set-up by removing the need for the long and bulky Hopkinson bars, the main advantage of this new paradigm is to relax the stringent assumptions on which the standard Split Hopkinson or Kolsky bars approaches rest. Indeed, the main idea is to use ultra-high speed imaging to record deformation maps as a function of time, using either speckle patterns and DIC or grids with phase shifting. From these data, strain maps can be derived by spatial differentiation and acceleration maps by double temporal differentiation. Using integral mechanical equilibrium, it is therefore possible to balance internal stresses calculated from strains and constitutive law with inertial forces obtained from the acceleration maps and the density. In this case, the need for external load measurement is relieved and all the required information is contained in the camera images, provided that the material density is known. The inertial effects, far from being a nuisance as in the standard SHPB/Kolsky approach, become an advantage by providing an imbedded distributed load cell. As a consequence of the above, the design space for test configurations opens up dramatically and needs to be explored as widely as possible in order to reach suitable new standard tests using this new paradigm. The target time for this is at least 10 years as this new design space is very large and test techniques will need to be adapted to the different classes of materials (brittle, ductile, soft, stiff etc.).

This paper has reached several important conclusions to advance the current topic.

- It is possible to reach sufficient deformation and acceleration levels with a purely inertial impact test as that of Fig. 2, with projectile speeds of 20 to 30 $m.s^{-1}$.
- There is enough information to extract the two stiffness components of an isotropic material. In fact, results have also shown that it was possible to use this test to identify the four in-plane orthotropic stiffness components of a composite (not reported here), so this simple test does have some mileage.
- Probably the major conclusion from this work is that recent progress in the technology of ultra-high speed cameras now enables collection of full-field deformation information of an unprecedented quality. It is also thought that while applications of full-field measurements at high strain rate develop, this market will grow, drawing in more technological development leading to further improved cameras. The current authors are of the opinion that at the horizon of about 5 years, ultra-high speed imaging will become nearly as common as high speed imaging currently is.
- Finally, the quality of the identification data is impressive at that level of strain rate, about 2000 s^{-1}. The two elastic stiffness components of a quasi-isotropic laminate have been

retrieved successfully, emphasizing the previous point about camera progress.

Clearly, this work is seminal in nature and only scratches the surface of the problem as many issues need to be addressed in the near and not so near future, a few of which are listed below.

- For the moment, the strain rate dependence of the stiffness has not been included in the identification. This is currently under implementation and will have to be validated first with numerical simulations. The first experimental investigation, also underway, concerns the strain rate dependence of the in-plane shear modulus of composites.
- Clearly, the identification of non-linear laws is the main objective for such a new paradigm to be successful. The feasibility of this using the VFM has already been proved in [4] but without inertia effects. In fact, non-linear laws present a somewhat easier situation as strain levels are usually higher and data contents richer.
- It is essential to understand the importance of all test parameters, including the imaging, data processing (grid pitch, smoothing, field of view etc.) on the identified quantities. An extension of the simulator developed in [46] will be used in the future to address this issue.
- The design space for test configuration needs to be explored in more depth. The current test is simple and was designed by intuitive thinking. There is a need for a more rational approach of test design. The identification simulator [46] mentioned above can be used for test design optimization with an objective of minimal bias on the identified parameters, taking into account as many test parameters as needed to make it realistic. This is a long-term task and a difficult problem as the identification chain is very long and involves very many parameters.
- Finally, there is a need for better constitutive models for high strain rate behaviour of materials. This has mainly been hindered by the poorer experimental evidence that could be collected compared to quasi-static situations. It is hoped that by improving test data, mechanics of materials researchers will be able to use this to develop better material models to take full-advantage of the extraordinary current and future capacities of numerical simulation.

This is an exciting time for high strain rate testing.

Acknowledgment

The authors would like to thank Brian Speyer from Speyer Photonics Ltd for the lending of the Shimadzu HPV-X camera. The funding of Haibin Zhu by the Chinese Scholarship Council is also gratefully acknowledged. C.R. Siviour thanks R. Duffin and W. Mix for designing and building the gas gun fixtures.

7 Supplementary material

- Video 1: Two components of the displacement field for the test with the Shimadzu HPV-X camera (file name: HPV-X_spec20_disp.avi)
- Video 2: Two components of the acceleration field for the test with the Shimadzu HPV-X camera (file name: HPV-X_spec20_accel.avi)
- Video 3: Three components of the strain field for the test with the Shimadzu HPV-X camera (file name: HPV-X_spec20_strain.avi)
- Video 4: Two components of the displacement field for the test with the SIMX16 camera (file name: SIM16_QI_disp.avi)
- Video 5: Two components of the acceleration field for the test with the SIMX16 camera camera (file name: SIM16_QI_accel.avi)
- Video 6: Three components of the strain field for the test with the SIMX16 camera camera (file name: SIM16_QI_strain.avi)
- Video 7: Strain rate in the x-direction for the test with the Shimadzu HPV-X camera (file name: HPV-X_spec20_strain_rate_x.avi)

References

[1] S. Aloui, R. Othman, A. Poitou, P. Guégan, and S. El-Borgi. Non-parametric identification of the non-homogeneous stress in high strain-rate uni-axial experiments. *Mechanics Research Communications*, 35(6):392–397, 2008.

[2] S. Avril, M. Grédiac, and F. Pierron. Sensitivity of the virtual fields method to noisy data. *Computational Mechanics*, 34(6):439–452, 2004.

[3] S. Avril and F. Pierron. General framework for the identification of elastic constitutive parameters from full-field measurements. *International Journal of Solids and Structures*, 44(14-15):4978–5002, 2007.

[4] S. Avril, F. Pierron, M. A. Sutton, and J. Yan. Identification of viscoplastic parameters and characterization of Lüders behaviour using digital image correlation and the virtual fields method. *Mechanics of Materials*, 40(9):729–742, 2008.

[5] C. Badulescu, M. Grédiac, and J. D. Mathias. Investigation of the grid method for accurate in-plane strain measurement. *Measurement Science and Technology*, 20(9), 2009.

[6] G. Besnard, F. Hild, J. M. Lagrange, P. Martinuzzi, and S. Roux. Analysis of necking in high speed experiments by stereocorrelation. *International Journal of Impact Engineering*, 49:179–191, 2012.

[7] B. Erzar and P. Forquin. An experimental method to determine the tensile strength of concrete at high rates of strain. *Experimental Mechanics*, 50:941–955, 2010.

[8] T. G. Etoh and H. Mutoh. An image sensor of 1 Mfps with photon counting sensitivity. volume 5580, pages 301–307, 2005.

[9] J.E. Field, S.M. Walley, W.G. Proud, H.T. Goldrein, and C.R. Siviour. Review of experimental techniques for high rate deformation and shock studies. *International Journal of Impact Engineering*, 30:725–775, 2004.

[10] P. Forquin. A new processing of spalling-tests to characterize the dynamic strength of geomaterials, 2013. Proceedings of the SEM 2013 annual conference, Lombard IL, USA.

[11] A. Gilat, T. E. Schmidt, and A. L. Walker. Full field strain measurement in compression and tensile split Hopkinson bar experiments. *Experimental Mechanics*, 49(2):291–302, 2009.

[12] A. Giraudeau, F. Pierron, and B. Guo. An alternative to modal analysis for material stiffness and damping identification from vibrating plates. *Journal of Sound and Vibration*, 329(10):1653–1672, 2010.

[13] S. G. Grantham, C. R. Siviour, W. G. Proud, and J. E. Field. High strain rate brazilian testing of an explosive simulant using speckle metrology. *Measurement Science and Technology*, 15(9):1867–1870, 2004.

[14] M. Grédiac, N. Fournier, P. A. Paris, and Y. Surrel. Direct identification of elastic constants of anisotropic plates by modal analysis: Experimental results. *Journal of Sound and Vibration*, 210(5):643–659, 1998.

[15] M. Grédiac and P. A. Paris. Direct identification of elastic constants of anisotropic plates by modal analysis: Theoretical and numerical aspects. *Journal of Sound and Vibration*, 195(3):401–415, 1996.

[16] M.A. Herraez, D.R. Burton, M.J. Lalor, and M.A. Gdeisat. Fast two-dimensional phase-unwrapping algorithm based on sorting by reliability following a non-continuous path. *Applied Optics*, 41(35):7437–7444, 2002.

[17] B. Hopkinson. A method of measuring the pressure produced in the detonation of high explosives of by the impact of bullets. *Philosophical Transactions of the Royal Society London A*, 213:437–456, 1914.

[18] J. Kajberg, K. G. Sundin, L. G. Melin, and P. Ståhle. High strain-rate tensile testing and viscoplastic parameter identification using microscopic high-speed photography. *International Journal of Plasticity*, 20(4-5):561–575, 2004.

[19] J. Kajberg and B. Wikman. Viscoplastic parameter estimation by high strain-rate experiments and inverse modelling - speckle measurements and high-speed photography. *International Journal of Solids and Structures*, 44(1):145–164, 2007.

[20] H. Koerber, J. Xavier, and P. P. Camanho. High strain rate characterisation of unidirectional carbon-epoxy IM7-8552 in transverse compression and in-plane shear using digital image correlation. *Mechanics of Materials*, 42(11):1004–1019, 2010.

[21] H. Kolsky. An investigation of the mechanical properties of materials at very high rates of loading. *Philosophical Transactions of the Royal Society London B*, 62:676–700, 1949.

[22] M. Longana. *Intermediate-strain rate testing methodologies and full-field optical strain measurement techniques for composite materials characterisation.* PhD thesis, University of Southampton, 2013. To be submitted.

[23] H. Luo, G. Churu, E. F. Fabrizio, J. Schnobrich, A. Hobbs, A. Dass, S. Mulik, Y. Zhang, B. P. Grady, A. Capecelatro, C. Sotiriou-Leventis, H. Lu, and N. Leventis. Synthesis and characterization of the physical, chemical and mechanical properties of isocyanate-crosslinked vanadia aerogels. *Journal of Sol-Gel Science and Technology*, 48(1-2):113–134, 2008.

[24] H. Luo, H. Lu, and N. Leventis. The compressive behavior of isocyanate-crosslinked silica aerogel at high strain rates. *Mechanics of Time-Dependent Materials*, 10(2):83–111, 2006.

[25] S. P. Mates, A. M. Forster, D. Hunston, R. Rhorer, R. K. Everett, K. E. Simmonds, and A. Bagchi. Identifying the dynamic compressive stiffness of a prospective biomimetic elastomer by an inverse method. *Journal of the Mechanical Behavior of Biomedical Materials*, 14:89–100, 2012.

[26] D. Mohr, G. Gary, and B. Lundberg. Evaluation of stress-strain curve estimates in dynamic experiments. *International Journal of Impact Engineering*, 37:161–169, 2010.

[27] R. Moulart, F. Pierron, S.R. Hallett, and M.R. Wisnom. Full-field strain measurement and identification of composites moduli at high strain rate with the virtual fields method. *Experimental Mechanics*, 51(4):509–536, 2011.

[28] J. Mullins, P. Hodgson, and T. Hilditch. Stress response of advanced high strength steels using tapered tensile specimens and digital image correlation method. pages 457–470, 2007.

[29] R. Muthupillai, D. J. Lomas, P. J. Rossman, J. F. Greenleaf, A. Manduca, and R. L. Ehman. Magnetic resonance elastography by direct visualization of propagating acoustic strain waves. *Science*, 269(5232):1854–1857, 1995.

[30] J. Niemczura and K. Ravi-Chandar. On the response of rubbers at high strain rates-I. simple waves. *Journal of the Mechanics and Physics of Solids*, 59(2):423–441, 2011.

[31] D. Notta-Cuvier, B. Langrand, E. Markiewicz, F. Lauro, and G. Portemont. Identification of johnson-cook's viscoplastic model parameters using the virtual fields method: Application to titanium alloy Ti6Al4V. *Strain*, 49(1):22–45, 2013.

[32] S.A. Novikov and A.V. Chernov. Determination of the spall strength from measured values of the specimen free surface velocity. *Zhurnal Prikladnoi Mekhaniki i Tekhnicheskoi Fiziki*, 23(5):703–705, 1982.

[33] S.A. Novikov, I.I. Divnov, and A.G. Ivanov. The study of fracture of steel, aluminium and copper under explosive loading. *Fizika Metallov i Metallovedeniye*, 21(4):607–615, 1966.

[34] R. Othman, S. Aloui, and A. Poitou. Identification of non-homogeneous stress fields in dynamic experiments with a non-parametric method. *Polymer Testing*, 29(5):616–623, 2010.

[35] J. Peirs, P. Verleysen, J. Degrieck, and F. Coghe. The use of hat-shaped specimens to study the high strain rate shear behaviour of Ti-6Al-4V. *International Journal of Impact Engineering*, 37(6):703–714, 2010.

[36] J. Peirs, P. Verleysen, W. Van Paepegem, and J. Degrieck. Determining the stress-strain behaviour at large strains from high strain rate tensile and shear experiments. *International Journal of Impact Engineering*, 38(5):406–415, 2011.

[37] F. Pierron, R. Cheriguene, P. Forquin, R. Moulart, M. Rossi, and M. Sutton. Performances and limitations of three ultra high-speed imaging cameras for full-field deformation measurements. volume 70, pages 81–86. 2011.

[38] F. Pierron and P. Forquin. Ultra high speed full-field deformation measurements on concrete spalling specimens and stiffness identification with the virtual fields method. *Strain*, 28(5):388–405, 2012.

[39] F. Pierron and M. Grédiac. *The virtual fields method. Extracting constitutive mechanical parameters from full-field deformation measurements.* Springer New-York, 2012.

[40] F. Pierron, B. Green, and M. R. Wisnom. Full-field assessment of the damage process of laminated composite open-hole tensile specimens. part I: methodology. *Composites Part A: Applied Science and Manufacturing*, 38(11):2307–2320, 2007.

[41] F. Pierron, M. A. Sutton, and V. Tiwari. Ultra high speed DIC and virtual fields method analysis of a three point bending impact test on an aluminium bar. *Experimental Mechanics*, 51(4):537–563, 2011.

[42] J. L. Piro and M. Grédiac. Producing and transferring low-spatial-frequency grids for measuring displacement fields with moiré and grid methods. *Experimental Techniques*, 28(4):23–26, 2004.

[43] P. L. Reu and T. J. Miller. The application of high-speed digital image correlation. *Journal of Strain Analysis for Engineering Design*, 43(8):673–688, 2008.

[44] S. Ri, M. Fujigaki, and Y. Morimoto. Sampling moiré method for accurate small deformation distribution measurement. *Experimental Mechanics*, 50(4):501–508, 2010.

[45] A. J. Romano, J. A. Bucaro, R. L. Ehman, and J. J. Shirron. Evaluation of a material parameter extraction algorithm using mri-based displacement measurement. *IEEE Transactions on Ultrasonics Ferroelectrics and Frequency Control*, 47(6):1575–1581, 2000.

[46] M. Rossi and F. Pierron. On the use of simulated experiments in designing tests for material characterization from full-field measurements. *International Journal of Solids and Structures*, 49(3-4):420–435, 2012.

[47] R. Sinkus, J. L. Daire, B. E. Van Beers, and V. Vilgrain. Elasticity reconstruction: Beyond the assumption of local homogeneity. *Comptes Rendus - Mecanique*, 338(7-8):474–479, 2010.

[48] C. R. Siviour. A measurement of wave propagation in the split Hopkinson pressure bar. *Measurement Science and Technology*, 20(6), 2009.

[49] M.A. Sutton, J.-J. Orteu, and H. Schreier. *Image correlation for shape, motion and deformation measurements.* Springer New-York, 2009.

[50] V. Tarigopula, O. S. Hopperstad, M. Langseth, A. H. Clausen, and F. Hild. A study of localisation in dual-phase high-strength steels under dynamic loading using digital image correlation and FE analysis. *International Journal of Solids and Structures*, 45(2):601–619, 2008.

[51] G.I. Taylor. The testing of materials at high rates of loading. *Journal of the Institute of Civil Engineering*, 26:486–519, 1946.

[52] V. Tiwari, M. A. Sutton, and S. R. McNeill. Assessment of high speed imaging systems for 2D and 3D deformation measurements: Methodology development and validation. *Experimental Mechanics*, 47(4):561–579, 2007.

[53] S.M. Walley. Special issue celebrating Hopkinson's centinary: editorial. *Philosophical Transactions of the Royal Society A*, 2014. In press.

[54] D. Wang, M. Lucas, and E. Tanner. Characterising the strain and temperature fields in a surrogate bone material subject to power ultrasonic excitation. *Strain*, 2013. In. press.

[55] Z. G. Wang and L. W. Meyer. On the plastic wave propagation along the specimen length in SHPB test. *Experimental Mechanics*, 50(7):1061–1074, 2010.

[56] E. Wielewski, M.R. Arthington, C.R. Siviour, S. Carter, F. Hofmann, A. M. Korsunsky, and N. Petrinic. A method for the in-situ measurement of evolving elliptical cross-sections in initially cylindrical Taylor impact specimens. *Journal of Strain Analysis for Engineering Design*, 45:429–437, 2010.

List of Figures

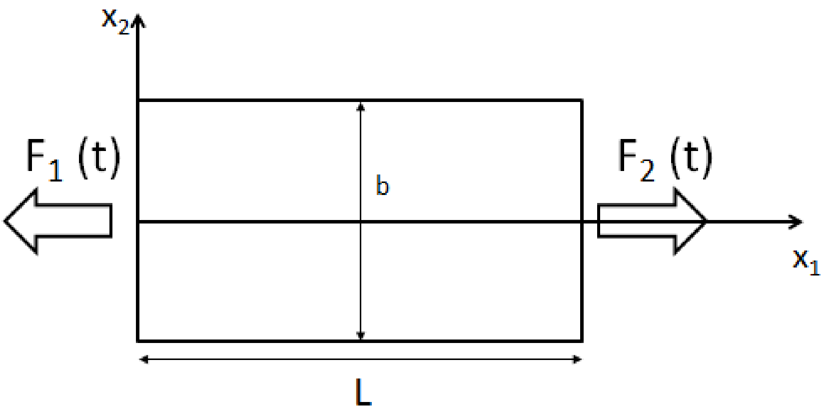

Figure 1: Schematic of a dynamic uniaxial test

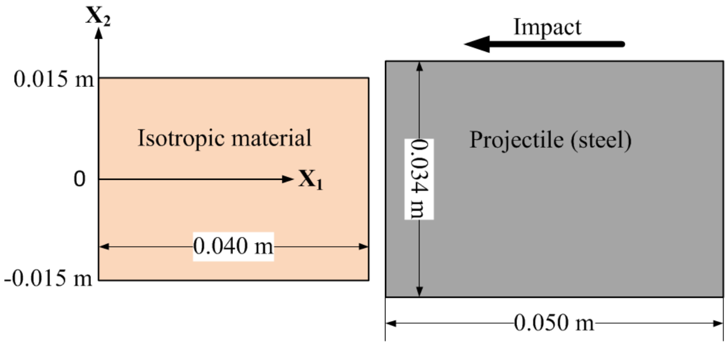

Figure 2: The schematic of impact model with straight projectile. Isotropic materials: $\rho = 2.2 \times 10^3 kg/m^3, E = 47.5\ GPa, \nu = 0.307$.

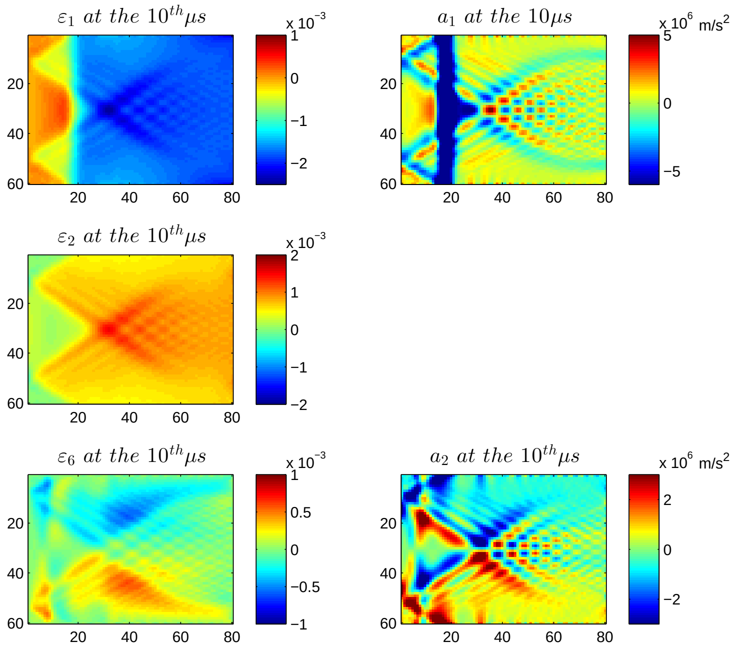

ε_1 at the $10^{th}\mu s$

a_1 at the $10\mu s$

ε_2 at the $10^{th}\mu s$

ε_6 at the $10^{th}\mu s$

a_2 at the $10^{th}\mu s$

Figure 3: Maps of full-field strain and acceleration fields at 10 μs

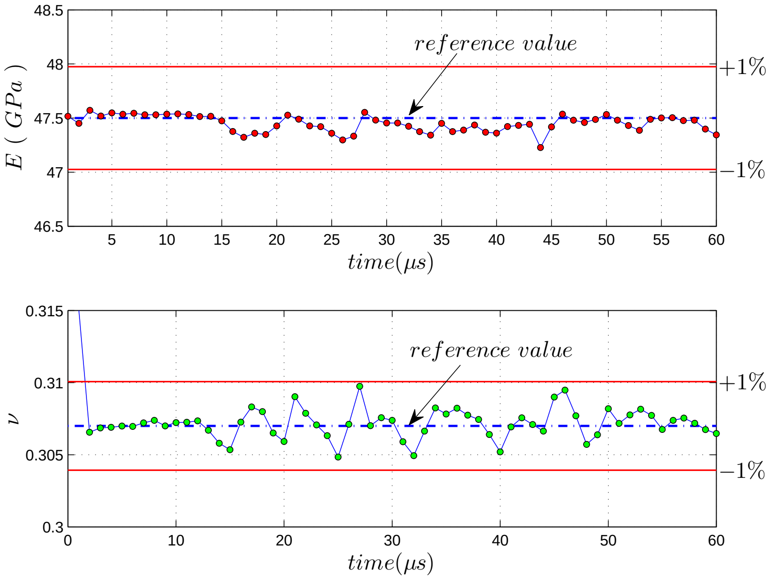

Figure 4: Identification of Young's modulus and Poisson's ratio from the simulated data. Data points: 80×60. $m = 4, n = 3$.

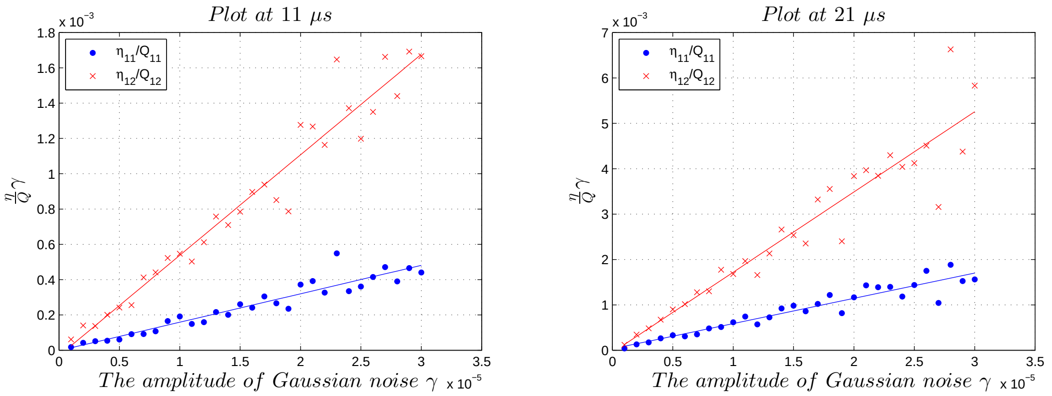

$Fitted\ \frac{\eta_{11}}{Q_{11}}$ =16.1139 $Theoretical\ \frac{\eta_{11}}{Q_{11}}$ =16.3169
$Fitted\ \frac{\eta_{12}}{Q_{12}}$ =56.9321 $Theoretical\ \frac{\eta_{12}}{Q_{12}}$ =55.2985

$Fitted\ \frac{\eta_{11}}{Q_{11}}$ =55.6232 $Theoretical\ \frac{\eta_{11}}{Q_{11}}$ =58.8946
$Fitted\ \frac{\eta_{12}}{Q_{12}}$ =176.8613 $Theoretical\ \frac{\eta_{12}}{Q_{12}}$ =180.0734

Figure 5: Plots of the coefficients of variations of the identified stiffnesses components for 1-dimension inertial model. Data fitted by linear regression. Data points: 80 × 60. Virtual mesh: $m = 4,\ n = 3$.

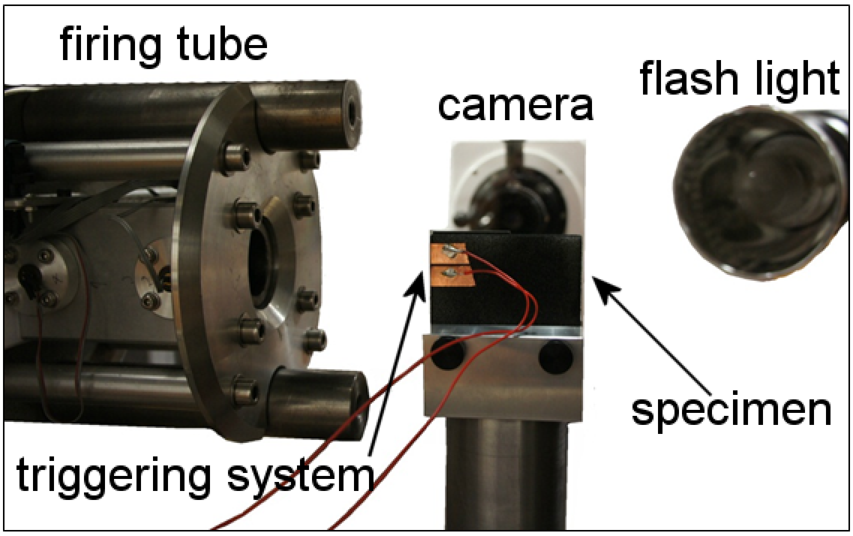

Figure 6: Experimental set-up for the inertial impact tests.

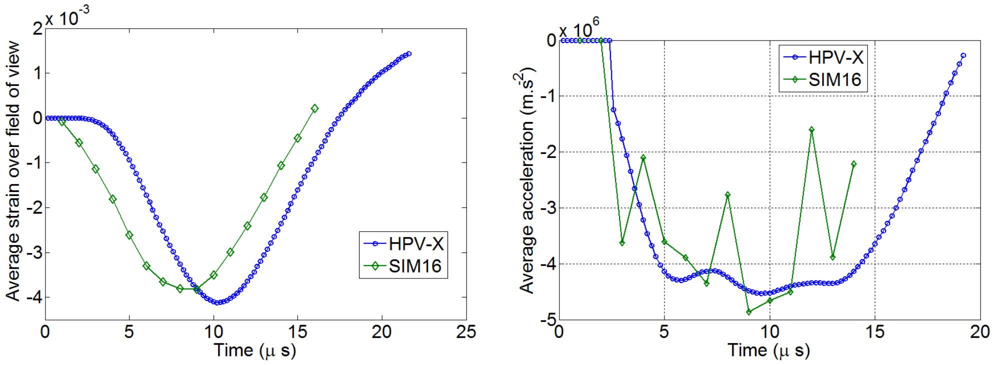

(A) Average strain $\overline{\varepsilon_1}$ (B) Average acceleration $\overline{a_1}$

Figure 7: Average ε_1 strain and a_1 acceleration for both cameras.

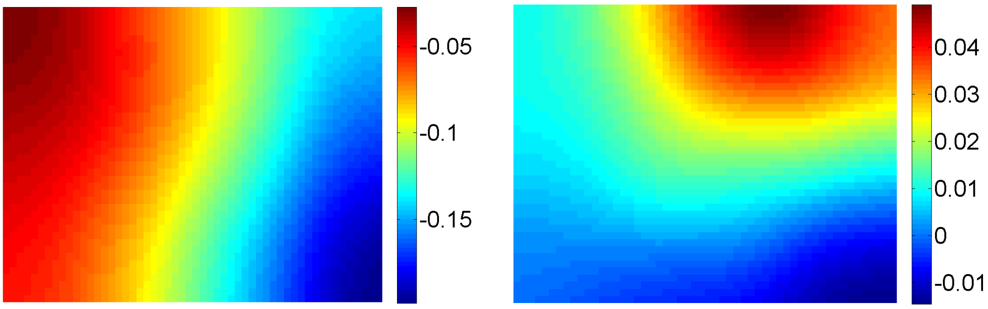

(A) U_1 at 10 μs, HPV-X (B) U_2 at 10 μs, HPV-X

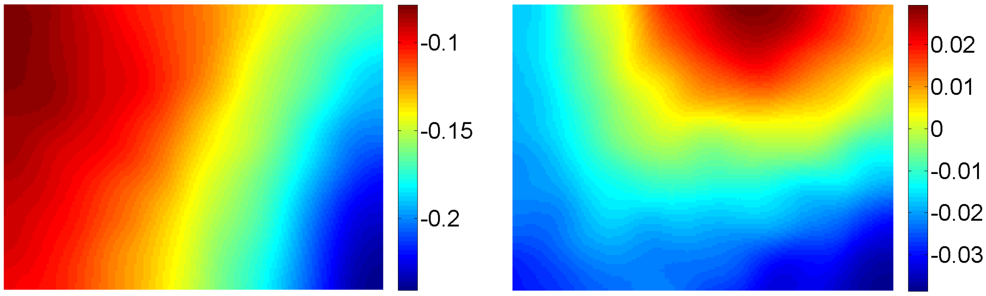

(C) U_1 at 8 μs, SIMX16 (D) U_2 at 8 μs, SIMX16

Figure 8: Displacement maps in mm for both cameras at 8 and 10 μs.

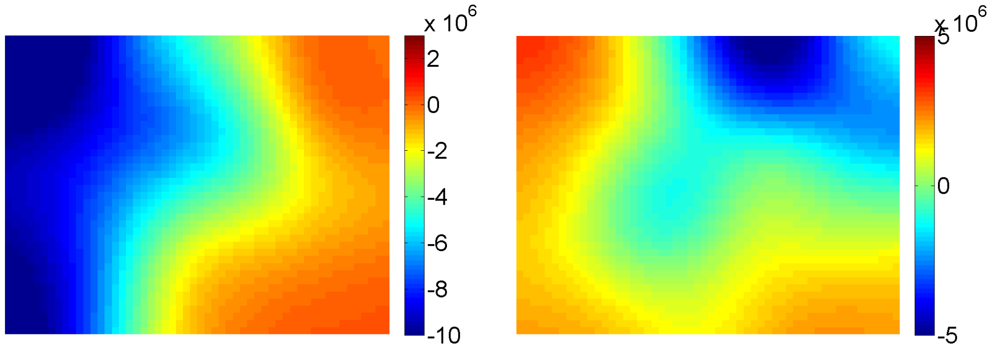

(A) a_1 at 10 μs, HPV-X (B) a_2 at 10 μs, HPV-X

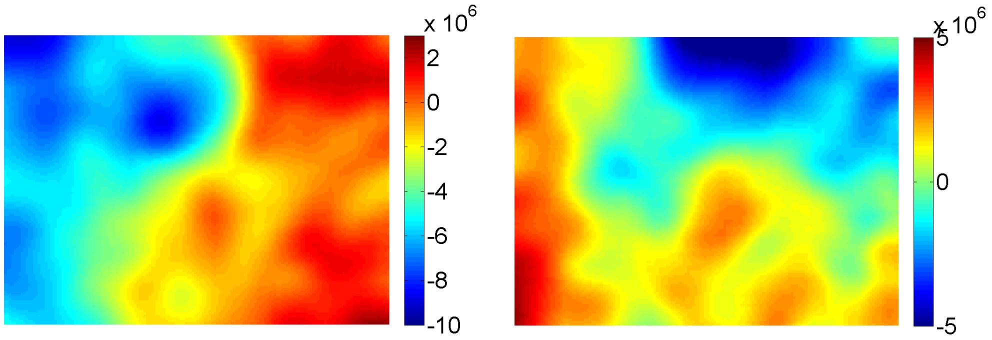

(C) a_1 at 8 μs, SIMX16 (D) a_2 at 8 μs, SIMX16

Figure 9: Acceleration maps in $m.s^{-2}$ for both cameras at 8 and 10 μs.

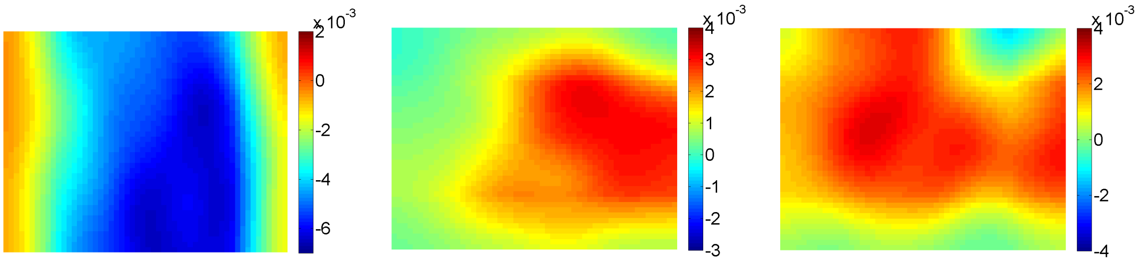

(A) ε_1 at 10 μs, HPV-X (B) ε_2 at 10 μs, HPV-X (C) ε_6 at 10 μs, HPV-X

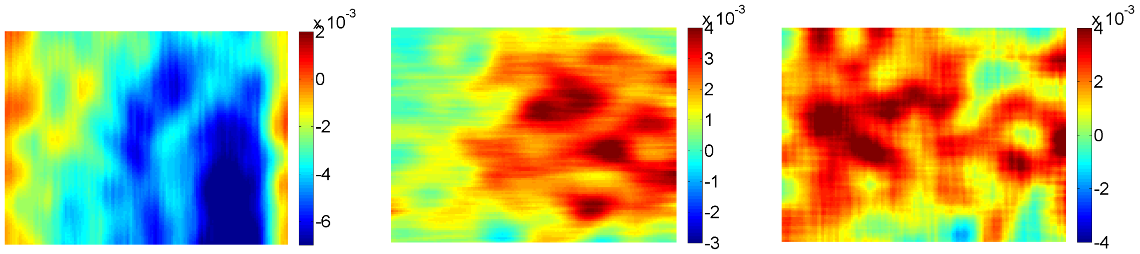

(D) ε_1 at 8 μs, SIMX16 (E) ε_2 at 8 μs, SIMX16 (F) ε_6 at 8 μs, SIMX16

Figure 10: Strain maps for both cameras at 8 and 10 μs.

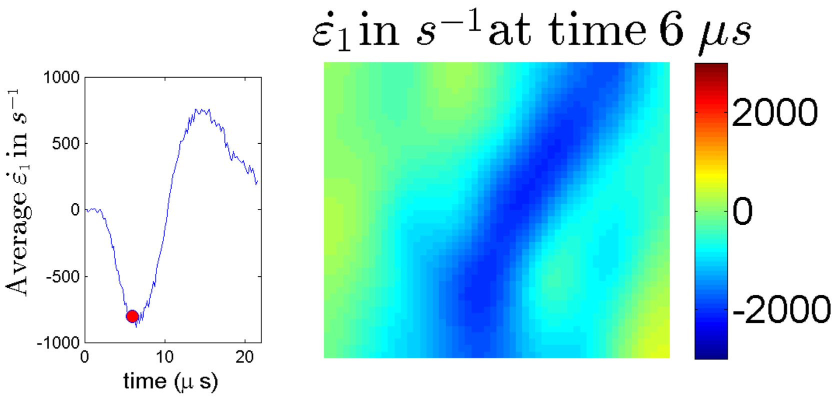

Figure 11: $\dot{\varepsilon_1}$ strain rate map at 6 μs for the HPV-X camera.

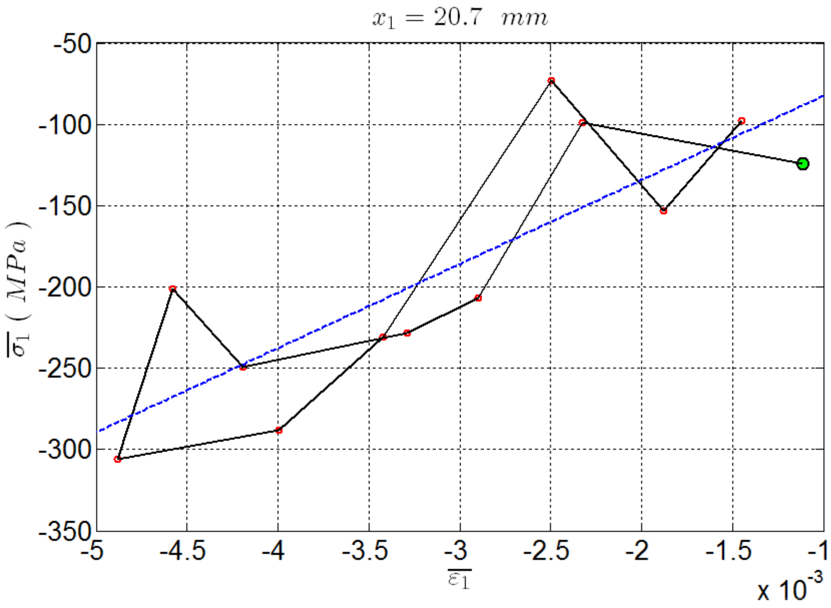

Figure 12: Stress-strain curves for the SIMX16 test.

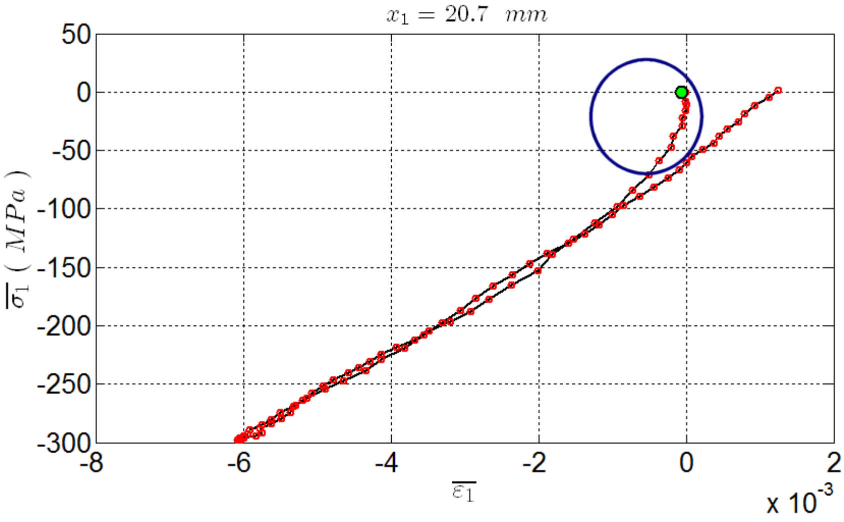

(A) Full stress-strain curve

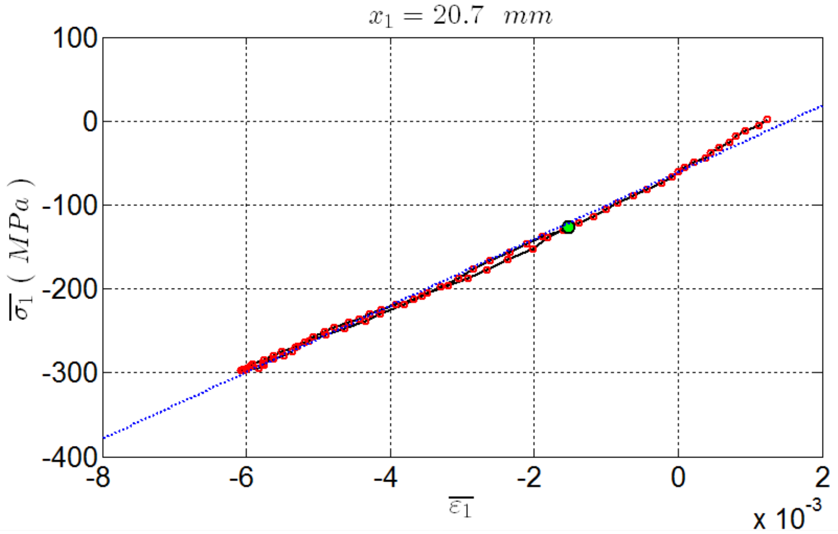

(B) Stress-strain curve without initial part and with linear fit

Figure 13: Stress-strain curves for the HPV-X test.

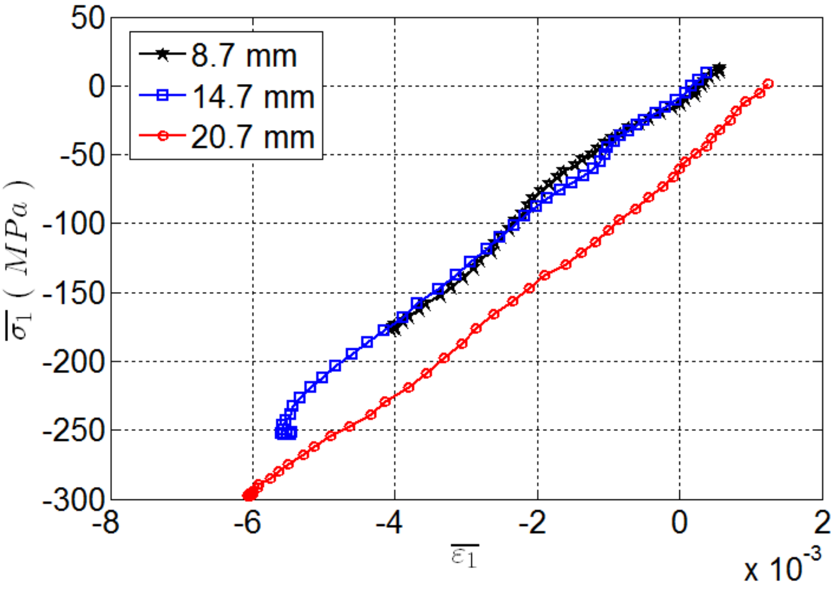

(A) Uniaxial stress assumption

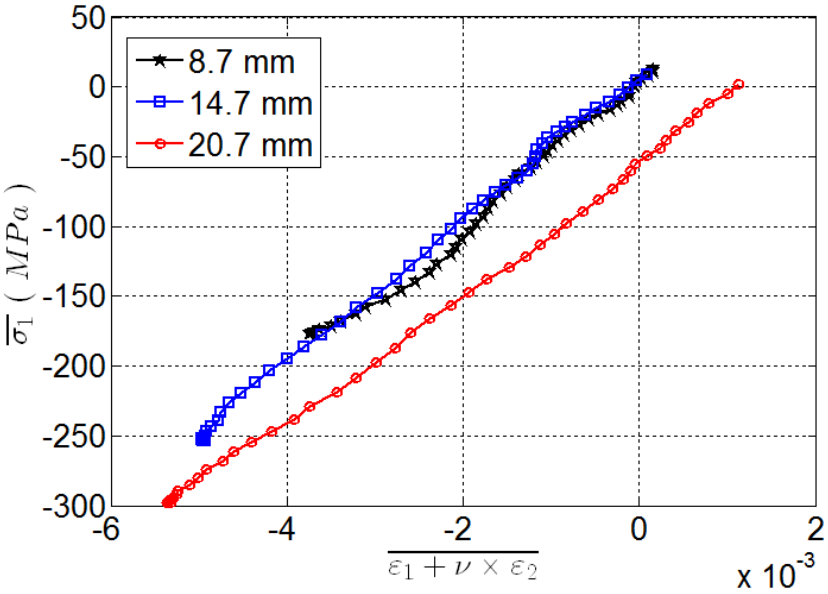

(B) No uniaxial stress assumption

Figure 14: Stress-strain curves at different locations for the HPV-X test.

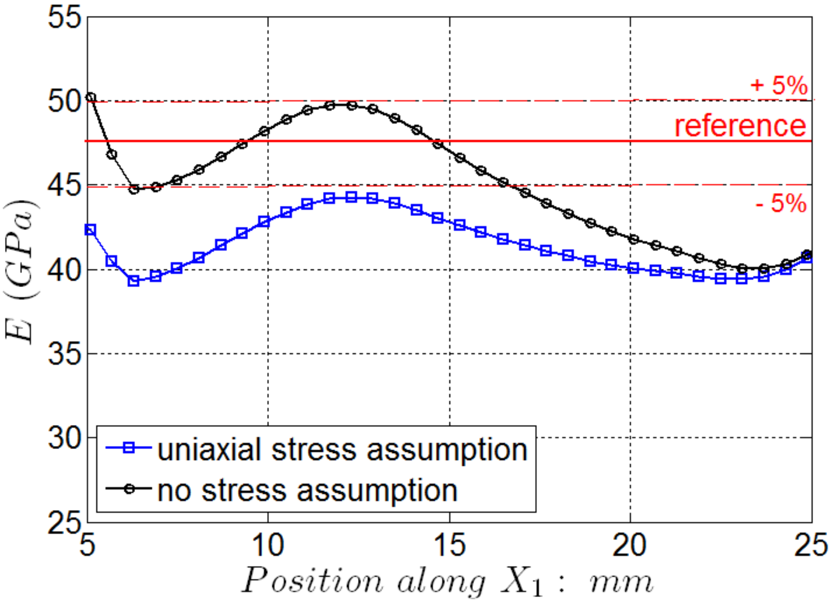

Figure 15: Modulus obtained from stress-strain curves with and without uniaxial stress assumption, HPV-X camera.

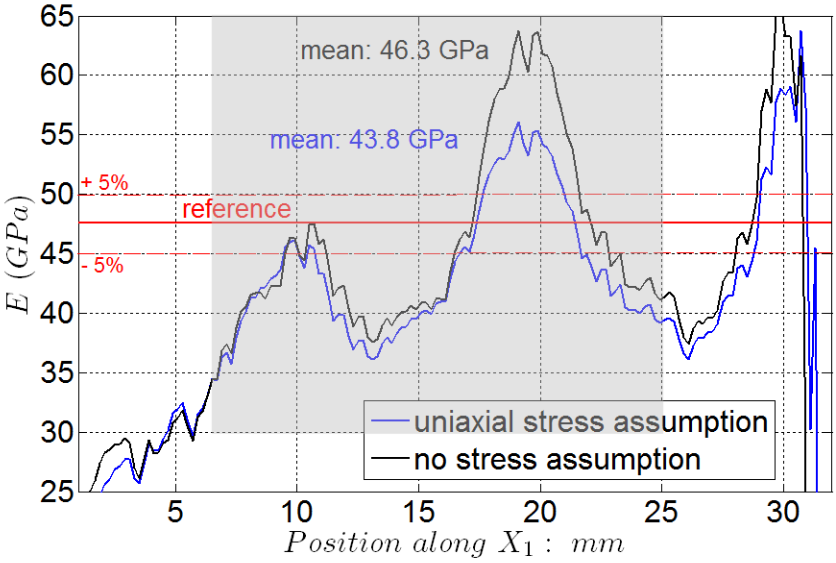

Figure 16: Modulus obtained from stress-strain curves with and without uniaxial stress assumption, SIMX16 camera.

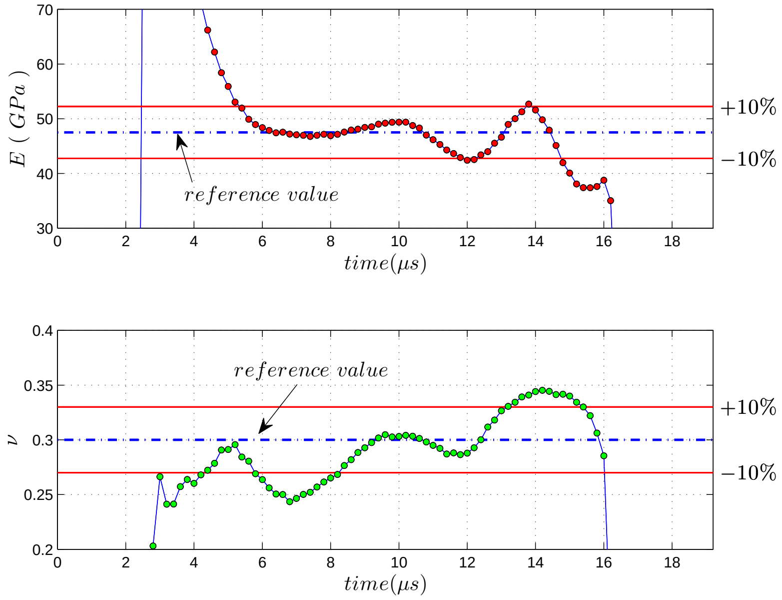

Figure 17: Identification results from the VFM, 10 x 2 virtual mesh, HPV-X camera.

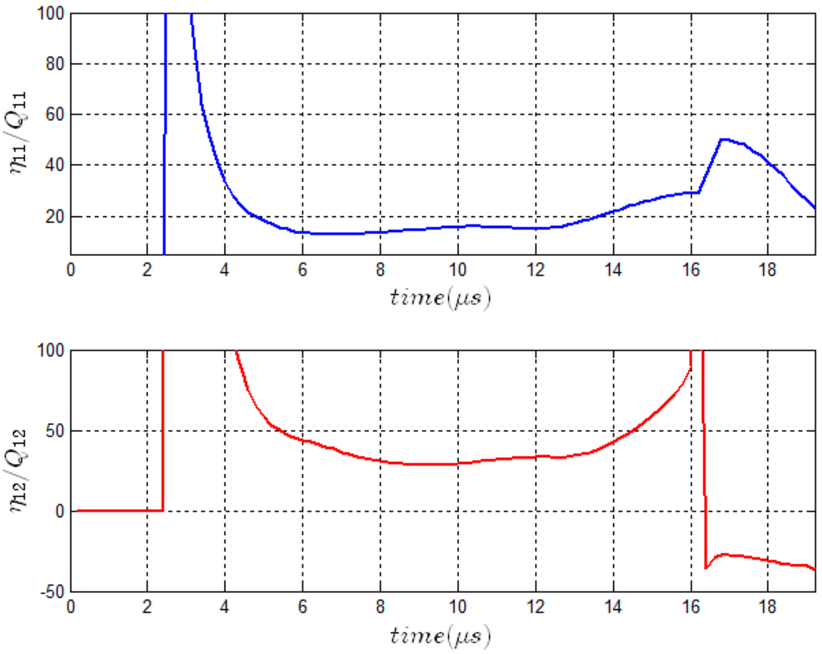

Figure 18: η_{ij} parameters for the VFM, 10 x 2 virtual mesh, HPV-X camera.

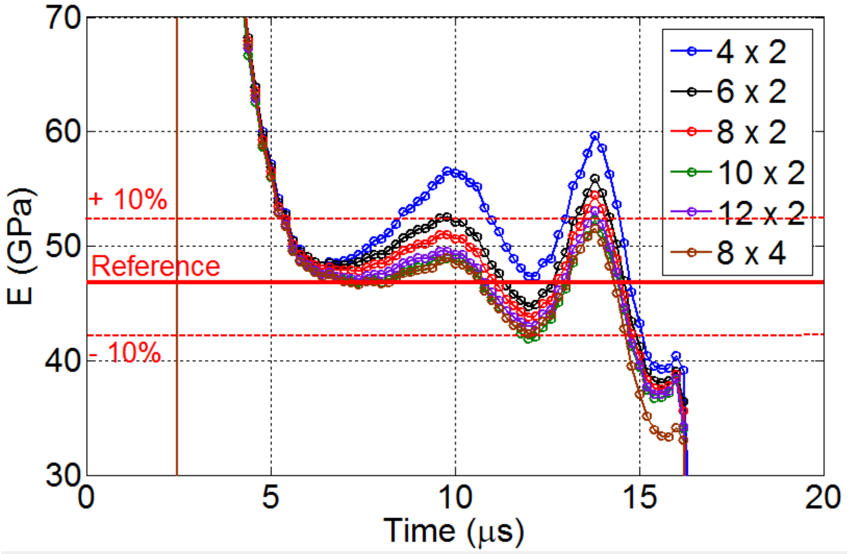

Figure 19: Identified E for the VFM, with several virtual mesh densities, HPV-X camera.

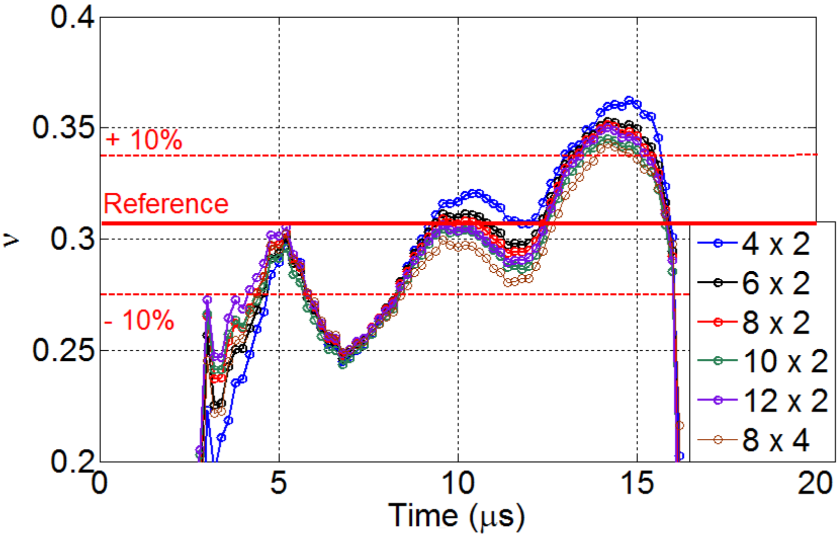

Figure 20: Identified ν for the VFM, with several virtual mesh densities, HPV-X camera.

Table 1: Details for the ABAQUS/EXPLICIT model

Mesh size	$5 \times 10^{-4}\ m$
Element type	$\boldsymbol{CPS4R}^{*}$
Inter-frame time	$1\ \mu s$
Contact type	Hard contact
Impact speed	$10\ m.s^{-1}$

*: 4-node bilinear plane stress quadrilateral, reduced integration, hourglass control

Table 2: Imaging and measurement performance information

	Specialized Imaging SIMX16	Shimadzu HPV-X
Pixel array size	1280 x 960	400 x 250
Interframe time (μs)	1	0.2
Number of images	16	128
Pitch of the grid	0.2 mm	0.6 mm
Sampling (pixels/period)	6	5
Field of view (data)	32.4 x 24.0 mm	32.0 x 25.2 mm
Raw displacement resolution	10 % of grid pitch	0.15 % of grid pitch
Spatial smoothing	Gaussian 16 x 16 data points	Gaussian, 9 x 9 then 10 x 10 data points
Temporal smoothing	3rd order polynomial over 5 μs	3rd order polynomial over 5 μs
Strain resolution (μ strain)	700	30
Acceleration resolution ($m.s^{-2}$)	5.10^5	2.10^4